

Anharmonicity-induced phonon hardening and anomalous thermal transport in ScZnXianyong Ding^{1,2}, Xin Jin³, Zheng Chang⁴, Dengfeng Li⁵, Xiaoyuan Zhou², Xiaolong Yang^{1,2,*} and Rui Wang^{1,2,†}¹*Institute for Structure and Function & Department of Physics, Chongqing University, Chongqing 400044, People's Republic of China*²*Center of Quantum materials and devices, Chongqing University, Chongqing 400044, People's Republic of China*³*College of Physics and Electronic Engineering, Chongqing Normal University, Chongqing 401331, People's Republic of China*⁴*School of Naval Architecture and Maritime, Zhejiang Ocean University, Zhoushan, Zhejiang, 316022, China*⁵*School of Science, Chongqing University of Posts and Telecommunications, Chongqing, 400065, China*

(Received 22 May 2024; revised 3 July 2024; accepted 18 July 2024; published 5 August 2024)

Phonon anharmonicity plays a crucial role in the lattice dynamics and lattice thermal conductivity κ_L of solids. Here, by combining first-principles calculations with the linearized Boltzmann transport equation, we unveil that phonon anharmonicity can make an unexpected contribution to κ_L and thereby lead to anomalous thermal transport behavior in the intermetallic compound ScZn, a recently theoretically predicted topological phonon material. We explicitly consider phonon renormalization, four-phonon (4ph), and phonon-electron scattering to predict the κ_L of ScZn. The results show that anharmonic phonon renormalization due to quartic anharmonicity gives rise to significant phonon hardening, especially for heat-carrying acoustic phonons. We also reveal that anharmonic effects largely decrease the fourth-order force constants, causing the dramatic suppression of 4ph scattering on κ_L . The incorporation of renormalization-induced phonon hardening and the decrease of quartic force constants makes a consequence of an almost twofold increase in the κ_L compared to the conventional harmonic treatment, from 3.9 to 7.6 W/mK at room temperature. This is enabled by the suppressed phonon scattering phase space and weakened fourth-order lattice anharmonicity due to the temperature-induced phonon renormalization effect. Moreover, it is found that the electronic contribution κ_e always plays a dominating role on the thermal conductivity; however, the lattice contribution is still considerable, leading to the substantial deviation of Lorenz number from the Sommerfeld value. This work provides a fundamental understanding of the thermal transport in ScZn and highlights the importance of anharmonic effects on the phonon energies and thermal conductivity of metals.

DOI: [10.1103/PhysRevB.110.054304](https://doi.org/10.1103/PhysRevB.110.054304)**I. INTRODUCTION**

Thermal transport is fundamentally important for a wide range of applications including energy conversion, heat management, and thermal barrier coatings [1–4]. It was generally believed that heat is mostly carried by phonons in nonmetallic solids, while in metals electrons overwhelmingly dominate the thermal conductivity (κ) and phonons have a negligible contribution. Recently, numerous transition intermetallic compounds and group-VI metals [5–8] have been identified to display an unusually high lattice (phonons) thermal conductivity (κ_L) at room temperature, comparable to or even larger than their electronic counterpart (κ_e). Notably, theoretical studies [9,10] predicted that the metallic compound TaN possesses an ultrahigh thermal conductivity primarily due to the contribution of phonons, and under moderate pressures (20–70 GPa), its κ can even surpass that of BAs, one of the best heat conductors. These studies have stimulated the investigation of anomalous heat transport in metals. The anomalously large κ_L in these metals is found to be highly associated with the unique combination of phononic and electronic structure [9] such as large frequency gap between acoustic and

optical branches, acoustic bunching, and the low electronic density of states (DOS) near the Fermi level, which gives rise to weak phonon-phonon and electron-phonon interactions. On account of the considerable phononic contribution to κ , these metals usually have a Lorenz number $L = \kappa/\sigma T$, where T is temperature and σ is the electrical conductivity, significantly larger than the Sommerfeld value $L_0 = \pi^2 k_B^2/3e^2 = 2.445 \times 10^{-8} \text{ V}^2/\text{deg}^2$. Therefore, it is rather challenging to experimentally separate the phononic and electronic contributions to κ of these metals via the Wiedemann-Franz law (WFL) using a presumed Lorenz number L_0 , although it works well for many conventional metals. This difficulty in experiment underscores the importance of establishing a theoretical understanding of the phononic and electronic thermal transport of metals in this category.

In the last decade, significant advancements in theoretical and computational efforts have been made to probe phonon-phonon, phonon-impurity, and electron-phonon interactions and their impact on various fundamental transport phenomena. Until now, parameter-free first-principles calculations in conjunction with the Peierls-Boltzmann transport equation (PBTE) have led to fundamental insights on thermal transport in solids and enabled accurate prediction of contributions to κ from both electrons and phonons [3,11–13]. In metals, the intrinsic κ_L is determined by anharmonic phonon-phonon scattering and phonon scattering by electrons

*Contact author: yangxl@cqu.edu.cn

†Contact author: rcwang@cqu.edu.cn

(hereafter “phonon-electron scattering”), while the intrinsic electronic contribution is limited by the scattering of electrons by phonons, or “electron-phonon scattering.” Within the harmonic approximation (HA) framework, the phonon linewidths and κ_L of numerous materials have been predicted accurately and understood reasonably when considering higher-order four-phonon scattering in addition to the lowest order of anharmonicity (three-phonon scattering) [14–18]. Moreover, recent studies [19–26] have shown that anharmonic phonon renormalization effect at finite temperatures plays a crucial role in determining the phonon energy, linewidth, and κ_L , especially for materials with strong anharmonicity or at high temperatures. Although the research techniques of accurately predicting thermal conductivity of metals are gradually maturing, thermal transport properties of a large number of metallic compounds with unique electronic or phononic structures, such as topological materials, remain less explored.

In this work, we conduct a comprehensive study of the phononic and electrical thermal transport properties of ScZn utilizing first-principles-based linearized PBTEs. ScZn, an intermetallic compound with a B2 lattice structure, was recently predicted to have coexisted nodal-line and nodal-ring topological phonons (TPs) [27]. However, a thorough and fundamental understanding of the intrinsic thermal transport in ScZn, which may be closely connected to its rich TPs, has yet to be established. By performing self-consistent phonon (SCP) calculations that include effects from bubble and loop diagrams, we show that anharmonic phonon renormalization induces a significant phonon hardening of the phonon dispersion at elevated temperatures, due to the strong fourth-order phonon anharmonicity. Employing the temperature-dependent harmonic and anharmonic force constants, we predict the κ_L of ScZn in the temperature range of 200–800 K, by considering three-phonon (3ph), four-phonon (4ph), isotope, and ph-el scatterings. Notably, we find that incorporating the anharmonic effects induced by temperature leads to significant enhancement in the κ_L , with a twofold increase of κ_L at room temperature. This is due to the combined effects of anharmonic phonon frequency renormalization and decreased fourth-order force constants with temperature, which severely suppress phonon scattering rates of heat-carrying acoustic phonons by altering the scattering phase space and anharmonic interaction matrix elements. Furthermore, by solving the electron PBTE, we also predict the phonon-limited electrical conductivity σ and electronic thermal conductivity κ_e . Our calculation shows that although κ_e always dominates the thermal conductivity throughout the temperature range, the lattice contribution is still significant, thereby leading to the substantial deviation of Lorenz number from the Sommerfeld value. Given that no experimental measurements of heat transport of ScZn have been reported, our theoretical prediction provides a basis for future experimental verification.

II. METHODOLOGY

A. First-principles calculations

The phonon frequencies and anharmonic interatomic force constants (IFCs) are calculated by using density functional

theory (DFT) as implemented in the Vienna *ab initio* simulation package (VASP) [28,29]. The exchange and correlation function is treated by generalized gradient approximation with the Perdew-Burke-Ernzerhof functional (PBE) [30], with the plane-wave energy cutoff of 500 eV. The projector augmented wave method [31] is used to treat the Sc ($3p^6 3d^2 4s^1$) and Zn ($3d^{10} 4s^2$) shells as valence states. The HA harmonic IFCs, third-order IFCs, and fourth-order IFCs are obtained by the finite-difference method with the supercell of $4 \times 4 \times 4$, using PHONOPY [32], THIRDORDER [33], and FOURTHORDER [34] codes, respectively. The cutoff radii of 0.5 and 0.2 nm are considered for third-order IFCs and fourth-order IFCs, respectively. The electron energies are calculated within density functional perturbation theory (DFPT) by the QUANTUM ESPRESSO package [35], where the interaction between the ionic and the valence electrons is described by ultrasoft pseudopotentials [36,37]. The cutoff energies for wave functions and charge densities are set to 60 and 600 Ry, respectively. The energy convergence threshold of 10^{-12} eV and a grid of $12 \times 12 \times 12$ \mathbf{k} points and $6 \times 6 \times 6$ \mathbf{q} points are used with the Monkhorst-Pack scheme. The electron-phonon Wannier (EPW) package [38] is employed to compute the electron-phonon coupling matrix elements with the coarse grids of $6 \times 6 \times 6$ for both \mathbf{k} and \mathbf{q} points, which are then interpolated into the dense $30 \times 30 \times 30$ for the calculation of phonon-electron (ph-el) scattering rates. Also, final grids of $65 \times 65 \times 65$ for both \mathbf{k} and \mathbf{q} points are used to calculate the electron-phonon (el-ph) scattering rates and κ_e via employing the PERTURBO code [39].

B. Anharmonic phonon renormalization and temperature-dependent force constants

The anharmonic renormalization effect on the phonon energies is incorporated by using SCP approximation method [40,41] as implemented in the ALAMODE package [41,42]. With only the first-order correction due to quartic anharmonicity (i.e., the loop diagram) is included, the SCP equation when neglecting the off-diagonal elements can be expressed as

$$\Omega_q^2 = \omega_q^2 + 2\Omega_q I_q, \quad (1)$$

where ω_q represents the harmonic phonon frequency at q , and Ω_q denotes the anharmonicity-renormalized phonon frequency at finite temperatures. The term I_q is defined as

$$I_q = \frac{1}{8N} \sum_{q'} \frac{V^{(4)}(q; -q; q', -q')}{4\Omega_q \Omega_{q'}} [1 + 2n(\Omega_{q'})], \quad (2)$$

where N , \hbar , n , and $V^{(4)}(q; -q; q'; -q')$ represent the number of uniformly sampled \mathbf{q} points, the reduced Planck constant, the phonon occupation number that obeys Bose-Einstein distribution, and the 4ph interaction strength, respectively. To provide more accurate prediction for the renormalized phonon frequencies, we further consider the off-diagonal terms of the phonon loop self-energy for polarization mixing (PM) [42], which were reported significant in certain crystal systems [25,43]. In the SCP calculations, the \mathbf{q} mesh is set to $4 \times 4 \times 4$ and the inner \mathbf{q}' is set to $4 \times 4 \times 4$. Recognizing that first-order SCP calculations solely yield renormalized

phonon energies originating from quartic anharmonicity, potentially leading to overestimation in highly anharmonic compounds [44,45], we also estimate additional negative frequency shifts stemming from cubic anharmonicity, i.e., the bubble diagram, within the quasiparticle approximation, utilizing the following self-consistent equation [44]:

$$(\Omega_q^B)^2 = \Omega_q^2 - 2\Omega_q \text{Re} \sum_q^B [G, \phi_3](\Omega_q^B), \quad (3)$$

where $\sum_q^B [G, \phi_3](\Omega_q)$ denotes the phonon frequency-dependent bubble self-energy, with B representing the bubble diagram, and ϕ_3 denotes the third-order IFCs included in the anharmonic self-energy calculation. Additionally, the temperature-dependent (TD) IFCs were derived using the finite-temperature effective potential method as implemented in the TDEP package [46,47]. Specifically, we utilize an efficient stochastic method for TDEP, eliminating the need for *ab initio* molecular dynamics [48]. Initially, we use the harmonic IFCs calculated at the ground state as starting points to generate snapshots of a $4 \times 4 \times 4$ supercell of ScZn at a specified temperature, by employing the *canonical_configuration* module of TDEP, which enables consideration of nuclear quantum effects [48]. Subsequently, we conduct a series of VASP forces and displacement calculations to extract the TD IFCs. The TDEP code can iteratively generate new IFCs from forces and displacements and new snapshots from IFCs until achieving self-consistency. Eventually, TD harmonic and anharmonic IFCs are obtained.

C. Phonon thermal conductivity

In the framework of the linearized phonon PBTE, the lattice thermal conductivity κ_L along the transport direction is expressed as

$$\kappa_L = \sum_{\lambda} C_{\lambda} v_{\lambda}^2 \tau_{\lambda}, \quad (4)$$

where λ represents the phonon mode with the specific wave vector \mathbf{q} and frequency ω , and C_{λ} , v_{λ} , and τ_{λ} are the specific heat, phonon group velocity, and phonon lifetime, respectively. Here, τ_{λ} is obtained by accurately solving the PBTE with an iterative scheme starting with the relaxation time approximation (RTA), as implemented in the modified SHENGBTE package [22,33,34]. Within the RTA, the phonon scattering rate, inverse of τ_{λ} , is computed as the summation of contributions from anharmonic three-phonon (3ph, $1/\tau_{\lambda}^{3\text{ph}}$), four-phonon (4ph, $1/\tau_{\lambda}^{4\text{ph}}$), phonon-isotope (ph-iso, $1/\tau_{\lambda}^{\text{iso}}$), and phonon-electron (ph-el, $1/\tau_{\lambda}^{\text{ph-el}}$) scattering processes through the Mattiessen's rule [49], expressed as

$$\frac{1}{\tau_{\lambda}} = \frac{1}{\tau_{\lambda}^{3\text{ph}}} + \frac{1}{\tau_{\lambda}^{4\text{ph}}} + \frac{1}{\tau_{\lambda}^{\text{iso}}} + \frac{1}{\tau_{\lambda}^{\text{ph-el}}}. \quad (5)$$

The phonon scattering terms resulting from 3ph, 4ph, ph-iso, and ph-el scatterings are given by [11,33,50,51]

$$\frac{1}{\tau_{\lambda}^{3\text{ph}}} = \sum_{\lambda'\lambda''} \left\{ \frac{1}{2} (1 + n_{\lambda'} + n_{\lambda''}) \Gamma_{-} + (n_{\lambda'} - n_{\lambda''}) \Gamma_{+} \right\}, \quad (6)$$

$$\frac{1}{\tau_{\lambda}^{4\text{ph}}} = \sum_{\lambda'\lambda''\lambda'''} \left\{ \frac{1}{6} \frac{n_{\lambda'} n_{\lambda''} n_{\lambda'''}}{n_{\lambda}} \Gamma_{---} + \frac{1}{2} \frac{(1 + n_{\lambda'}) n_{\lambda''} n_{\lambda'''}}{n_{\lambda}} \right. \\ \left. \times \Gamma_{+-} + \frac{1}{2} \frac{(1 + n_{\lambda'})(1 + n_{\lambda''}) n_{\lambda'''}}{n_{\lambda}} \Gamma_{+++} \right\}, \quad (7)$$

$$\frac{1}{\tau_{\lambda}^{\text{iso}}} = \sum_{\lambda'} \Gamma_{\text{iso}}, \quad (8)$$

$$\frac{1}{\tau_{\lambda}^{\text{ph-el}}} = \frac{2\Pi''_{\mathbf{q}\nu}}{\hbar}, \quad (9)$$

where Γ_{\pm} , $\Gamma_{\pm\pm}$, and Γ_{iso} are the scattering probability matrices for 3ph, 4ph, and ph-iso processes, respectively. $\Pi''_{\mathbf{q}\nu}$ represents the imaginary part of phonon self-energy, and ν signifies the phonon branches. These quantities are written as

$$\Gamma_{\pm} = \frac{\pi \hbar}{4N} |V_{\pm}^{(3)}|^2 \Delta_{\pm} \frac{\delta(\omega_{\lambda} \pm \omega_{\lambda'} - \omega_{\lambda''})}{\omega_{\lambda} \omega_{\lambda'} \omega_{\lambda''}}, \quad (10)$$

$$\Gamma_{\pm\pm} = \frac{\pi \hbar}{4N} \frac{\hbar}{2N} |V_{\pm\pm}^{(4)}|^2 \Delta_{\pm\pm} \frac{\delta(\omega_{\lambda} \pm \omega_{\lambda'} \pm \omega_{\lambda''} - \omega_{\lambda'''})}{\omega_{\lambda} \omega_{\lambda'} \omega_{\lambda''} \omega_{\lambda'''}}, \quad (11)$$

$$\Gamma_{\text{iso}} = \frac{\pi}{2N} \omega_{\lambda} \omega_{\lambda'} \sum_b^{\lambda} g_b |e_b^{\lambda} e_b^{\lambda'*}|^2 \delta(\omega_{\lambda} - \omega_{\lambda'}), \quad (12)$$

$$\Pi''_{\mathbf{q}\nu} = 2\pi \sum_{mn} \int_{\text{BZ}} \frac{d\mathbf{k}}{\Omega_{\text{BZ}}} |g_{mn,\nu}(\mathbf{k}, \mathbf{q})|^2 \\ \times [f_{n\mathbf{k}}(T) - f_{m\mathbf{k}+\mathbf{q}}(T)] \delta(\varepsilon_{m\mathbf{k}+\mathbf{q}} - \varepsilon_{n\mathbf{k}} - \omega). \quad (13)$$

In these expressions, Δ and δ ensure the momentum conservation and energy conservation of scattering processes. For 3ph processes, $+$ represents the absorption processes and $-$ the emission processes. As for 4ph processes, three types of scattering channels are involved, i.e., recombination ($++$), redistribution ($+ -$), and splitting ($--$) processes. Mass disorder can be quantified by $g_b = \sum_j f_{jb} (1 - m_{jb}/\bar{m}_b)^2$, where j denotes the isotope types, f_{jb} is the fraction of the isotope j , and \bar{m}_b is the average atom mass of the basis b sites. $f_{n\mathbf{k}}(T)$ represents the electronic occupation at wave vector \mathbf{k} and band indices n , $\varepsilon_{n\mathbf{k}}$ are the associated eigenvalues, and $g_{mn,\nu}(\mathbf{k}, \mathbf{q})$ represents the electron-phonon matrix element. The transition probability matrices $V_{\pm}^{(3)}$ and $V_{\pm\pm}^{(4)}$ are

$$V_{\pm}^{(3)} = \sum_{ijk} \sum_{\alpha\beta\gamma} \Phi_{ijk}^{\alpha\beta\gamma} \frac{e_{\alpha}^{\lambda}(i) e_{\beta}^{\pm\lambda'}(j) e_{\gamma}^{\mp\lambda''}(k)}{\sqrt{M_i M_j M_k}} e^{\pm i\mathbf{q}' \cdot \mathbf{r}_j} e^{-i\mathbf{q}'' \cdot \mathbf{r}_k}, \quad (14)$$

$$V_{\pm\pm}^{(4)} = \sum_{ijkl} \sum_{\alpha\beta\gamma\theta} \Phi_{ijkl}^{\alpha\beta\gamma\theta} \frac{e_{\alpha}^{\lambda}(i) e_{\beta}^{\pm\lambda'}(j) e_{\gamma}^{\pm\lambda''}(k) e_{\theta}^{\mp\lambda'''}(l)}{\sqrt{M_i M_j M_k M_l}} \\ \times e^{\pm i\mathbf{q}' \cdot \mathbf{r}_j} e^{\pm i\mathbf{q}'' \cdot \mathbf{r}_k} e^{-i\mathbf{q}''' \cdot \mathbf{r}_l}. \quad (15)$$

Here, $\Phi_{ijk}^{\alpha\beta\gamma}$ and $\Phi_{ijkl}^{\alpha\beta\gamma\theta}$ are the third- and fourth-order IFCs. e_{α}^{λ} denotes the phonon eigenvector and r_j is the position vector of the j th unit cell. i, j, k, l denote the atom indices and $\alpha, \beta, \gamma, \theta$ denote the directions.

D. Electronic thermal conductivity and electrical conductivity

The determination of electrical thermal conductivity (κ_e) and electrical conductivity (σ) involves solving the linearized electron PBTE. The electrical conductivity σ is defined as [11]

$$\sigma = \frac{2e^2}{N_{\mathbf{k}} V k_B T} \sum_{n\mathbf{k}} f_{n\mathbf{k}}^0 (1 - f_{n\mathbf{k}}^0) \mathbf{v}_{n\mathbf{k}} \otimes \mathbf{F}_{n\mathbf{k}}, \quad (16)$$

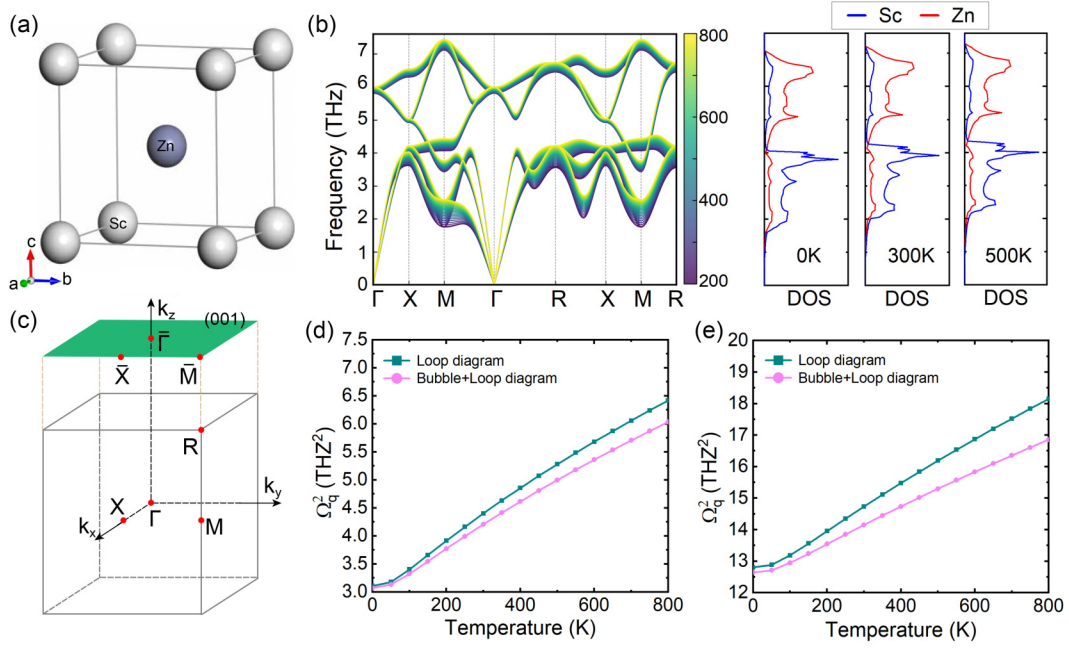


FIG. 1. (a) The crystal structure of ScZn (space group $Pm\bar{3}m$ 221). (b) Calculated temperature-dependent phonon dispersions from 200 to 800 K. The right panel gives the atom-decomposed partial phonon DOS at $T = 0, 300,$ and 500 K. (c) The first Brillouin zone (BZ) and the corresponding (001) surface BZ of ScZn. Calculated temperature-dependent squared phonon frequency of the lowest-lying acoustic phonon branch at the **M** (d) and **R** (e) points, respectively.

where e is the elementary charge, f_{nk}^0 is the equilibrium electron Fermi-Dirac distribution, and \mathbf{v}_{nk} is the electron group velocity. \mathbf{F}_{nk} is the electron mean-free path limited by el-ph scattering processes, which is exactly resolved using an iterative PBTE scheme [11,12]. The electronic thermal conductivity κ_e is given by [11]

$$\kappa_e = \frac{2}{N_{\mathbf{k}} V k_B T^2} \sum_{n\mathbf{k}} f_{n\mathbf{k}}^0 (1 - f_{n\mathbf{k}}^0) (E_{n\mathbf{k}} - E_f)^2 \mathbf{v}_{n\mathbf{k}} \otimes \mathbf{F}_{n\mathbf{k}} - T \sigma S^2, \quad (17)$$

with

$$\sigma S = \frac{2e}{N_{\mathbf{k}} V k_B T^2} \sum_{n\mathbf{k}} f_{n\mathbf{k}}^0 (1 - f_{n\mathbf{k}}^0) (E_{n\mathbf{k}} - E_f) \mathbf{v}_{n\mathbf{k}} \otimes \mathbf{F}_{n\mathbf{k}}, \quad (18)$$

where $E_{n\mathbf{k}}$ and E_f are the electronic energy and Fermi energy. The convergence of κ_e and σ concerning \mathbf{q} -points density is carefully tested and displayed in Fig. S3 of the Supplemental Material (SM) [52].

III. RESULTS AND DISCUSSION

A. Anharmonicity-induced phonon hardening

ScZn crystallizes in a body-centered-cubic (bcc) structure with a space group of $Pm\bar{3}m$ (No. 221), where the Sc and Zn atoms occupy the Wyckoff positions $1a$ (0, 0, 0) and $1b$ ($\frac{1}{2}, \frac{1}{2}, \frac{1}{2}$), respectively, as depicted in Fig. 1(a). We first investigate the phonon dispersion of ScZn using different levels of theory (HA and SCP calculations). The calculated HA phonon dispersion is shown in Fig. S1 of the SM [52], which is consistent with the literature [27] and does not exhibit any

imaginary frequencies in the whole BZ, indicating the dynamical stability of ScZn at the ground state. The anharmonically renormalized phonon dispersions from 200 to 800 K are displayed in Fig. 1(b). The overall phonon dispersion exhibits a pronounced hardening as temperature increases, especially for acoustic phonon modes in the frequency range of 2–4 THz in the vicinity of the **M** point and along **R-X** and **M-R** high-symmetry paths. These modes are primarily contributed by the vibrations of Sc atoms, as revealed in the atom-decomposed phonon DOS in the right panel of Fig. 1(b). In contrast, the higher-frequency optical phonons that are dominated by the vibrations of Zn atoms are slightly hardened with the increasing temperature. Given that most materials typically tend to exhibit phonon softening as the temperature increases [19,22], the overall hardening of the phonon spectrum in ScZn is unusual, which should be extremely important for the phonon transport of ScZn since it can affect the phonon group velocity, phonon scattering phase space, and consequently the κ_L .

Another thing worth mentioning is that a prior study [27] has revealed the coexistence of nodal-ring TPs composed of the band-crossing points near 4 THz and the nodal-line TPs along the ΓX and the ΓR directions, as marked in the phonon dispersion in Fig. 2(a). Since the topological properties are determined by the harmonic IFCs, whether the harmonic IFCs include anharmonic phonon renormalization could somehow affect these TPs. As is evident from the phonon dispersions at 0 and 300 K in Fig. 2(a), anharmonic phonon renormalization obviously hardens the phonon branches at 300 K, which causes the nodal-ring TPs to shift slightly towards higher frequency while the nodal-line TPs are unaffected. To further examine the influence of phonon renormalization effects on the TPs, we also calculate the topological phonon surface

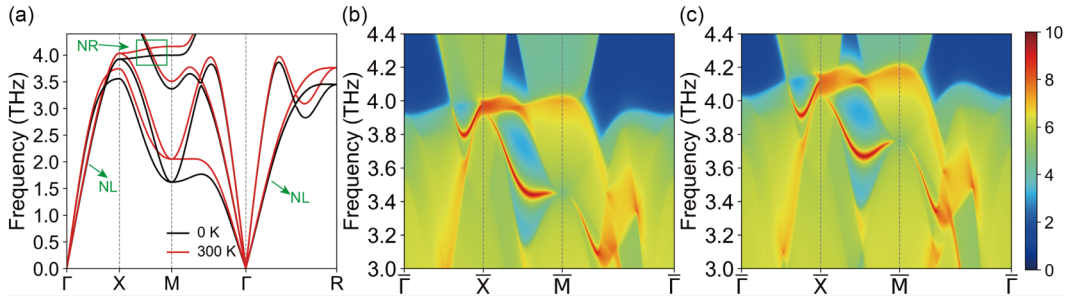


FIG. 2. (a) Phonon spectra of ScZn at 0 and 300 K, respectively. The surface phononic spectra of the (001) surface of ScZn at (b) 0 K and (c) 300 K, respectively.

states using the harmonic IFCs at 0 and 300 K, respectively. As displayed in Figs. 2(b)–2(c), the surface states at 300 K are similar to the case at 0 K except for an overall upward shift in the phonon frequency, indicating that the phonon renormalization effect enables the alteration of TPs in the energy space.

It is also important to note that both the third- and fourth-order anharmonicities are responsible for the accurate prediction of renormalized phonon frequencies, with the former (bubble diagram) contributing negative phonon frequency shifts whereas the latter (loop diagram) providing positive frequency shifts [21,23,25,26]. Hence, whether the phonon mode eventually exhibits softening or hardening should depend on the competition between the loop and bubble diagrams. To clarify their relative importance, we calculate the squared phonon frequency of the lowest-lying transverse acoustic (TA) phonon mode at the **M** and **R** points as a function of temperature, as shown in Figs. 1(d) and 1(e). It is evident that compared with the results calculated solely from the loop diagram, the resultant phonon frequency when further consideration of the bubble diagram, although being obviously suppressed, still shows a hardening behavior as temperature increases, indicating the predominance of quartic anharmonicity-induced phonon renormalization in determining the phonon frequency.

To understand the physics behind the anharmonicity-induced phonon hardening, we further calculate the potential energy surfaces (PESs) of the lowest-lying TA phonon mode at the **M** and **R** points, as illustrated in Figs. 3(a) and 3(b). It is clearly visible that both the TA modes show the U-

shaped PESs when atomic collective displacements increase at elevated temperatures, which largely deviate from the HA-contributed PESs. Notably, the U-shaped PESs of these modes can be matched well with the fourth-order polynomial as seen in the solid lines in Figs. 3(a) and 3(b), providing evidence for the strong quartic anharmonicity at finite temperatures. Besides, the strong anharmonic phonon hardening can also manifest in the atomic mean-square displacements (MSDs). From Fig. 3(c), we see that the calculated MSDs of both Sc and Zn atoms in the HA are significantly larger than those given by the SCP calculations at higher temperatures. This implies that strong quartic anharmonicity hardens the atom vibrations and thus suppresses the phonon population, leading to the decreased MSDs.

B. Anharmonic phonon renormalization effects significantly increases phonon thermal conductivity

We then examine the effect of anharmonic phonon renormalization on the lattice thermal conductivity κ_L of ScZn. As shown in Fig. S2 [52], κ_L reaches convergence when the **q**-point density is set to $12 \times 12 \times 12$, and this setting will be employed in the subsequent calculations. The κ_L values from 200 to 800 K are calculated using six levels of thermal transport theory with accuracy from low to high, as illustrated in Fig. 4(a). The lowest level of theory is the HA+3ph method, namely, calculating κ_L with only 3ph scattering included using all IFCs at the ground state, and the highest level of theory is the SCP+3,4ph method, that incorporates both 4ph scattering

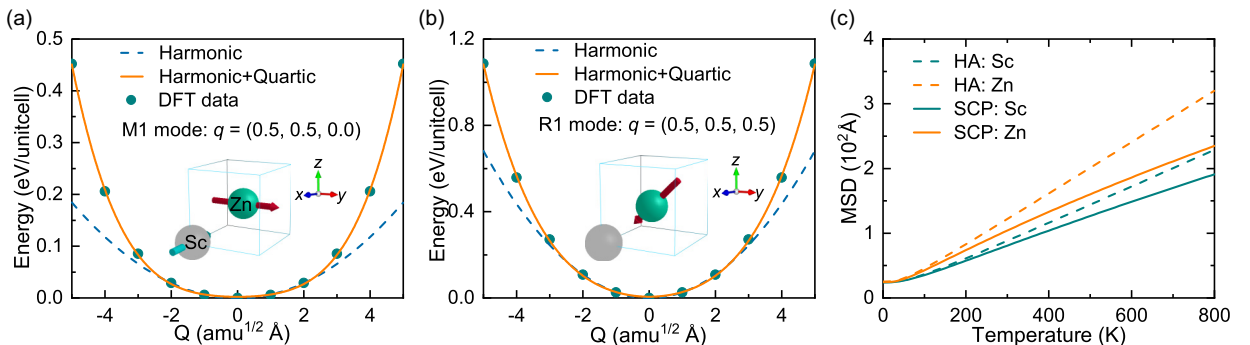


FIG. 3. Calculated potential energy surfaces (PESs) of the lowest-lying TA phonon mode at the **M** (a) and **R** (b) points. The insets denote the corresponding vibration modes. (c) Calculated atomic mean-square displacements (MSDs) as a function of temperature. The dashed and solid lines represent the results obtained from the HA and SCP calculations, respectively.

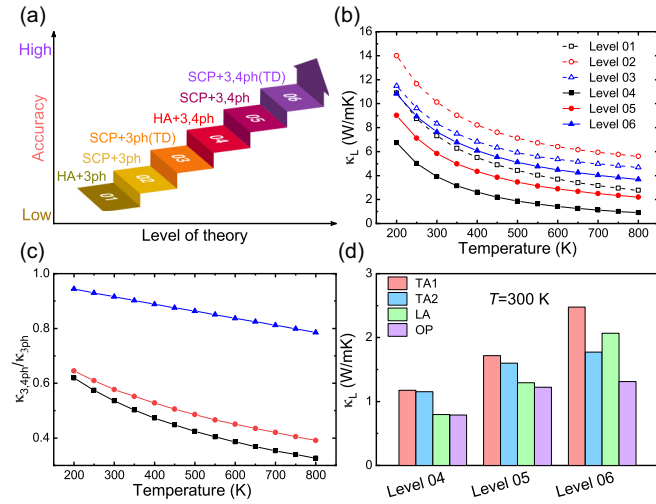


FIG. 4. (a) A schematic illustrating the hierarchical ladder of theories for calculating κ_L . The levels of theory with accuracy from low to high are HA+3ph, SCP+3ph, SCP+3ph(TD), HA+3,4ph, SCP+3,4ph, and SCP+3,4ph(TD), where the HA and SCP correspond to phonon frequencies without and with renormalization through the SCP theory, respectively, and 3/4ph denotes the calculated 3/4ph scattering rates using anharmonic IFCs at the ground state (0 K), and 3/4ph(TD) for scattering rates calculated with the TD anharmonic IFCs. (b) Temperature-dependent κ_L calculated at different levels of theory. (c) The ratio of $\kappa_{3,4ph}$ to κ_{3ph} as a function of temperature, where $\kappa_{3,4ph}$ and κ_{3ph} denote the κ_L values with and without inclusion of four-phonon scattering, respectively. (d) The branch contribution to κ_L at 300 K, predicted within the different levels of theory.

processes and phonon renormalization effects on all harmonic and anharmonic IFCs, while the other methods are a compromise between the two. Specifically, the SCP+3ph means that κ_L is calculated through 3ph scattering using the TD second-order IFCs combined with the third-order IFCs at 0 K, while the SCP + 3ph(TD) indicates that the κ_L is obtained using the TD second- and third-order IFCs. Similarly, the SCP+3,4ph represents the calculation when the 4ph scattering is included using the TD second-order IFCs and the anharmonic IFCs at 0 K. The calculated results are shown in Fig. 4(b), which convey three important insights. First, anharmonic phonon renormalization plays a crucial role in determining the κ_L as temperature increases, which can significantly enhance the κ_L . At room temperature, the predicted κ_L using the method III is 8.3 W/mK, 18% larger than that given by the method I, and as temperature rises to 800 K, the renormalization effect increases the κ_L by 43%, from 2.7 to 4.7 W/mK. Second, renormalization effects can greatly weaken the suppression of 4ph scattering on the κ_L . Specifically, at 300 K, including 4ph scattering by the method IV reduces the κ_L from 7.6 W/mK given by the method I to 3.9 W/mK, by 49%, and after consideration of renormalization effect on the fourth-order IFCs, 4ph scattering only reduces κ_L by about 8% from 8.3 W/mK given by the method III to 7.6 W/mK obtained from the method VI. Third, consideration of full temperature effects on anharmonic IFCs leads to remarkable improvement of κ_L . For instance, the predicted κ_L using the method VI that captures

anharmonic effects on all IFCs is 7.6 W/mK at 300 K, which is almost twice the one predicted by using ground-state all IFCs, namely, the method IV.

To highlight the importance of phonon renormalization effects and four-phonon scattering on the κ_L , Fig. 4(c) presents the temperature-dependent ratio of κ_L calculated with and without inclusion of four-phonon scattering, i.e., $\kappa_{3,4ph}/\kappa_{3ph}$, using different levels of theory. When the renormalization effects are not taken into account for all IFCs, four-phonon scattering severely suppresses the κ_L at elevated temperatures, e.g., by nearly 50% and 70% reduction at 300 and 800 K, respectively. If we only consider the temperature-induced renormalization effect on phonon dispersion, the suppression of κ_L by four-phonon scattering is obviously weakened, e.g., including four-phonon scattering reduces κ_L by $\sim 40\%$ at 300 K. This implies that phonon dispersion hardening effect reduces the number of allowed four-phonon scattering processes, thus promoting an increase in κ_L . Remarkably, employment of renormalized all-harmonic and anharmonic IFCs further greatly weakens the role of four-phonon scattering, giving rise to a reduction of less than 10% in κ_L at room temperature. That is, the renormalization effect significantly weakens phonon anharmonicity and thus increases the κ_L . By comparing the κ values obtained within the II and III levels of theory, it is found that κ_L obviously decreases when renormalized third-order IFCs are employed, indicating that the renormalization effect strengthens the third-order anharmonicity. This also suggests that the renormalization effects lead to the strong weakening of fourth-order phonon anharmonicity, which was also reported in other systems [22,53]. Hence, combining the above results, it can be concluded that the severe weakening effect of four-phonon scattering induced by renormalization effects on κ_L is enabled by the synergistic effect of phonon dispersion hardening and fourth-order anharmonicity softening, with the latter playing a leading role.

Further decomposing κ_L into different branches, we can see in Fig. 4(d) that the phonon renormalization effects bring about noticeable improvement of the contributions of each branch to κ_L , especially for three acoustic branches. At 300 K, when taking into account the renormalized phonon energies only, the κ_L contributed from the two transverse acoustic (TA) modes, denoted as TA1 and TA2, longitudinal acoustic (LA) modes, and optical (OP) modes are increased from 1.2, 1.1, 0.8, and 0.8 W/mK to 1.7, 1.6, 1.3, and 1.2 W/mK, by 41.7%, 45.4%, 62.5%, and 50%, respectively. With the further consideration of renormalized anharmonic IFCs, the contributions of TA1, TA2, LA, and OP modes to κ_L are improved to 2.5, 1.8, 2.0, and 1.3 W/mK, by 47.1%, 12.5%, 53.8%, and 8.3% compared to the case given by the level V of theory, respectively. Additionally, it is worth noting that the TA phonons contribute more than 50% to the κ_L , and a considerable number of TA modes are the nodal-line TPs along the ΓX and the ΓR directions as illustrated in Fig. 2(a), indicating that topological phonons have a significant contribution to κ_L .

For a clearer insight into the improvement of κ_L by the temperature-induced phonon renormalization, we compare the spectral thermal conductivities as a function of phonon frequency at 300 and 500 K, respectively, calculated from the different levels of theory. As seen in Fig. 5, the heat is mainly carried by phonons below 4 THz, corresponding to the

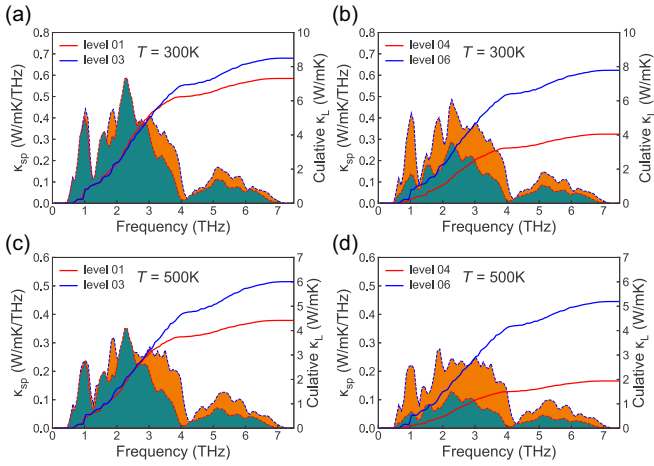


FIG. 5. (a) The cumulative and spectral κ_L of ScZn with respect to the phonon frequency calculated within different levels of theory at 300 K (a), (b), and 500 K (c), (d).

acoustic modes. With only the 3ph scattering included, the renormalization effects obviously increase the contribution of phonons above 4 THz to κ_L at 300 K and more so at 500 K, as proven in Figs. 5(a) and 5(c), indicating that phonon renormalization mainly affects the three-phonon limited κ_L contributed by high-frequency acoustic phonons and optical phonons. After incorporating 4ph scattering, it is seen from

Figs. 5(b) and 5(d) that the κ_L contributed from phonons throughout the frequency range is largely improved by renormalization effects, especially at 500 K, implying that the renormalization effects can substantially weaken the suppression effect of 4ph scattering on the contribution of all phonon modes to κ_L . These results further highlight the importance of full consideration of anharmonic phonon renormalization effects in determining the κ_L of ScZn.

C. Microscopic mechanisms governing the anharmonicity-enhanced phonon thermal conductivity

We next investigate the effect of phonon renormalization on the phonon transport properties of ScZn. Figure 6(a) gives the comparison of phonon specific heat calculated with the HA and SCP methods, which shows indistinguishable agreement with each other over the whole temperature region. Meanwhile, it is evident from Fig. 6(b) that consideration of phonon renormalization effect leads to the slight decrease in the group velocities of acoustic phonons (<4 THz), as compared to the HA results. This is because renormalization effect makes the acoustic branches flatter along certain high-symmetric paths, e.g., ΓM and RX directions, resulting in a slight decrease in the group velocities of certain acoustic modes as illustrated in the inset of Fig. 6(b). To quantify the influence of phonon renormalization on the harmonic thermal transport, we calculate the small-grain-limit thermal conductivity, defined as $\kappa_{SG} = \sum_{\lambda} C_{\lambda} v_{\lambda}$, which can measure

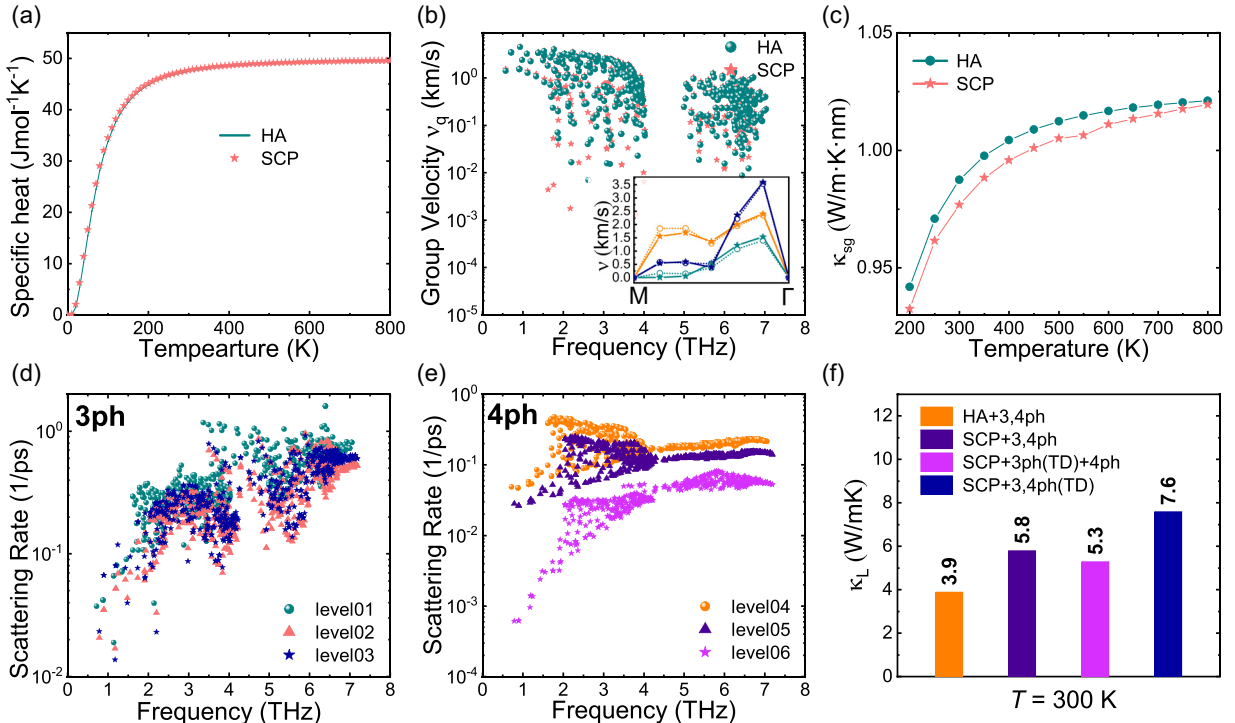


FIG. 6. (a) Temperature-dependent phonon specific heat with the SCP calculation in comparison with the HA results. (b) Modal phonon group velocities with and without consideration of anharmonic phonon renormalization at 300 K, respectively. The inset denotes the group velocities along M - Γ direction. The dotted lines denote the HA results and the solid lines denote the SCP results, in which the different colors of green, orange, and blue lines correspond to the TA1, TA2, and LA branches. (c) The calculated κ_{sg} with HA and SCP calculation as a function of temperature. (d) Three-phonon scattering rates and (e) four-phonon scattering rates calculated within different levels of theory at 300 K. (f) The calculated room-temperature κ_L from the mixed IFCs.

the contribution of harmonic properties to κ_L . As is seen in Fig. 6(c), when the temperature effect is taken into account, the resulting κ_{SG} decreases slightly over the entire temperature range, stemming from the decreased group velocity. The results suggest that renormalization effects at finite temperatures have a rather weak impact on the harmonic phonon transport properties. Hence, the prominent increase in κ_L due to the renormalization effects should be attributed to the change in the phonon lifetime, another key factor determining κ_L .

To this end, we plot the scattering rates of 3ph and 4ph processes calculated at different theoretical levels in Figs. 6(d) and 6(e). As expected, when the anharmonic correction to the phonon dispersion is incorporated, the 3ph scattering rates of all modes decrease obviously compared with the HA results. Further considering the modification of renormalization effects to the third-order IFCs, the overall 3ph scattering rates increase slightly, which is mainly due to the hardening of third-order anharmonicity as mentioned above. For 4ph processes, the renormalization effects are much stronger than for 3ph scattering, as clearly seen in Fig. 6(e). Similarly, including anharmonic correction to the phonon dispersion results in a noticeable decrease in the 4ph scattering rates of all modes. Notably, with further consideration of TD fourth-order IFCs, the 4ph scattering rates are decreased by almost an order of magnitude, demonstrating that the fourth-order anharmonicity is dramatically weakened by the renormalization effects. To quantify the effects of phonon renormalization on the harmonic and anharmonic IFCs, we also calculate the κ_L using the mixed IFCs. From Fig. 6(f), we notice that by employing the SCP phonon dispersion combined with the 0-K anharmonic IFCs, namely, the SCP+3,4ph model, the predicted κ_L at 300 K is increased from 3.9 W/mK given by the HA+3,4ph method to 5.8 W/mK. If the TD third-order IFCs are further used, i.e., the SCP+3ph(TD)+4ph model, κ_L is slightly reduced to 5.3 W/mK, which is consistent with the cubic anharmonicity hardening with increasing temperature. When full treatment of finite-temperature effects on all IFCs [the SCP+3, 4ph(TD)] is employed, the predicted κ_L is significantly increased to 7.6 W/mK, nearly twice as large as the value given by the HA+3,4ph model, indicating the predominance of the weakened quartic anharmonicity with temperature over the phonon frequency hardening in enhancing the κ_L .

The above analyses explicitly show that the increase in κ_L caused by the anharmonic effects originates from the decreased phonon scattering rates, particularly the 4ph scattering rates. The phonon scattering rate relies on the phase space and the transition probability matrix elements, both of which can be affected by renormalization effects. Therefore, it is necessary to elaborate on how the phonon renormalization affects these two factors separately. Figures 7(a) and 7(b) present the 3ph and 4ph scattering phase space contributed from different types of processes, calculated with the HA and SCP approaches. For 3ph scattering, the scattering rate is contributed by the absorption ($\lambda_1 + \lambda_2 \rightarrow \lambda_3$) and emission ($\lambda_1 \rightarrow \lambda_2 + \lambda_3$) processes. As is clearly evident in Fig. 7(a), the 3ph scattering rates of heat-carrying acoustic phonons (<4 THz) are dominated by the absorption processes, and both subprocesses are obviously suppressed by the anharmonic phonon renormalization due to the limitations of energy

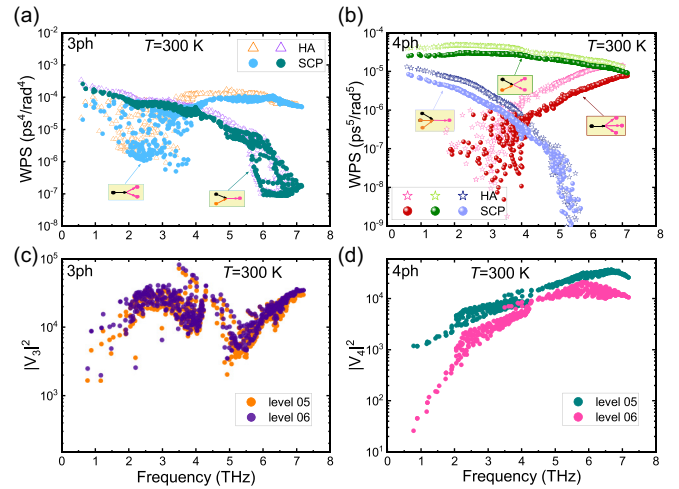


FIG. 7. (a) The weighted phase space (WPS) of 3ph scattering with the HA and SCP calculations at 300 K. (b) The WPS of 4ph scattering with the HA and SCP calculations at 300 K. (c) The transition probability matrix of 3ph processes $|V_{\pm}^{(3)}|^2$. (d) The transition probability matrix of 4ph processes $|V_{\pm}^{(4)}|^2$.

and momentum selective rules. Four-phonon scattering involves three sub-processes, i.e., recombination ($\lambda_1 + \lambda_2 + \lambda_3 \rightarrow \lambda_4$), redistribution ($\lambda_1 + \lambda_2 \rightarrow \lambda_3 + \lambda_4$), and splitting ($\lambda_1 \rightarrow \lambda_2 + \lambda_3 + \lambda_4$) channels. It is seen in Fig. 7(b) that the redistribution processes make a dominant contribution to the 4ph scattering rates for all modes, as broadly seen in other systems [15,54], and anharmonic corrections to the phonon dispersion significantly reduce the scattering channels of all three subprocesses. These results demonstrate that the decrease of phonon scattering rate by renormalization effects is partly due to the reduced scattering phase space. We then move on to the transition probability matrix elements, which can be used to characterize the phonon anharmonicity. Figure 7(c) shows the mode-resolved transition probability matrix elements of 3ph scattering, and the minor enlarged matrix elements after using the TD third-order IFCs provide direct evidence for the slight hardening of third-order anharmonicity with temperature. More noticeably, it is seen in Fig. 7(d) that treatment of anharmonicity correction to the fourth-order IFCs markedly reduces the 4ph scattering matrix elements, especially for low-frequency phonons below 2 THz, further confirming the weakened fourth-order anharmonicity with temperature. The above information conveys to us that the increased κ_L due to the anharmonic renormalization effects is a result of the prolonged phonon lifetime, which is enabled by the suppressed phonon scattering phase space and weakened quartic anharmonicity.

D. Anomalous thermal transport and large Lorenz number

Figure 8(a) shows the calculated electronic band structure and projected electron DOS, which reflect the metallic character of ScZn. For metals, the electron-phonon interaction (EPI) usually plays a crucial role in both thermal and electrical transport. To uncover the strength of EPI, we plot the Eliashberg spectral function $\alpha^2F(\omega)$ and corresponding el-ph coupling constant $\lambda(\omega)$ in Fig. 8(b). It is seen that

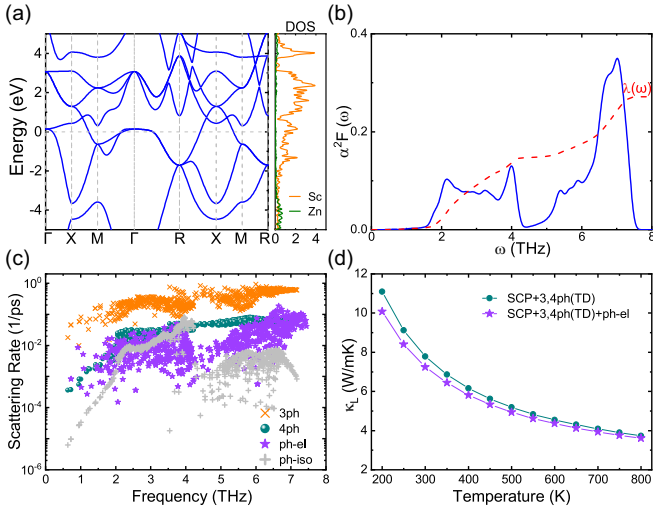


FIG. 8. (a) The electronic band structures and projected electron DOS of ScZn. (b) The Eliashberg spectral function $\alpha^2 F(\omega)$ and electron-phonon coupling strength $\lambda(\omega)$. (c) The comparison of 3ph, 4ph, ph-el, and isotope scattering rates at 300 K. (d) The calculated temperature-dependent κ_L with and without inclusion of ph-el scattering.

the $\alpha^2 F(\omega)$, which is associated with the phonon (electron) limited electron (phonon) scattering strength, is contributed by phonons with frequencies in the ranges of 2–4 and 4–8 THz, corresponding to the high-frequency acoustic phonons and all optical phonons, respectively. The saturated $\lambda(\omega)$ value is 0.28, which is comparable to the value of many other metals [55], indicating that the ph-el scattering is not negligible in determining the κ_L of ScZn. To see how the scattering of phonon by electron is important to κ_L , we compare the room-temperature ph-el scattering rates with the 3ph, 4ph, and isotope scattering rates in Fig. 8(c). It is clearly evident that the ph-el scattering rates are comparable to the 4ph scattering rates over the whole frequency range, both of which are much weaker than the 3ph counterparts. When including the ph-el scattering, the eventual κ_L is slightly lower than that given by the level VI of theory over the entire temperature regime, e.g., 4% reduction at 300 K, which reveals that the EPI has a rather weak effect on suppressing the κ_L .

In addition to κ_L , we also pay attention to the electronic thermal conductivity κ_e of ScZn, which is generally considered to be the leading contributor to thermal conductivity in metals. The calculated κ_e , the lattice component κ_L , and the total thermal conductivity $\kappa = \kappa_L + \kappa_e$ in the temperature range of 200–800 K are plotted in Fig. 9(b). As seen in the figure, the phonon limited κ_e is nearly temperature independent and has a value of 12.2 W/mK at 300 K. In analogy to common metals, the κ_e contributes to the majority of thermal conductivity in ScZn over the whole temperature range. Although the lattice contribution to κ is secondary, its contribution to thermal conductivity is still significant, especially at room temperature and below. At 300 K, the calculated κ_L is 7.6 W/mK, which is comparable to 60% of the electronic contribution, accounting for $\sim 38\%$ of κ .

We also study the electrical transport properties of ScZn. From Fig. 9(a), it can be seen that the calculated electrical

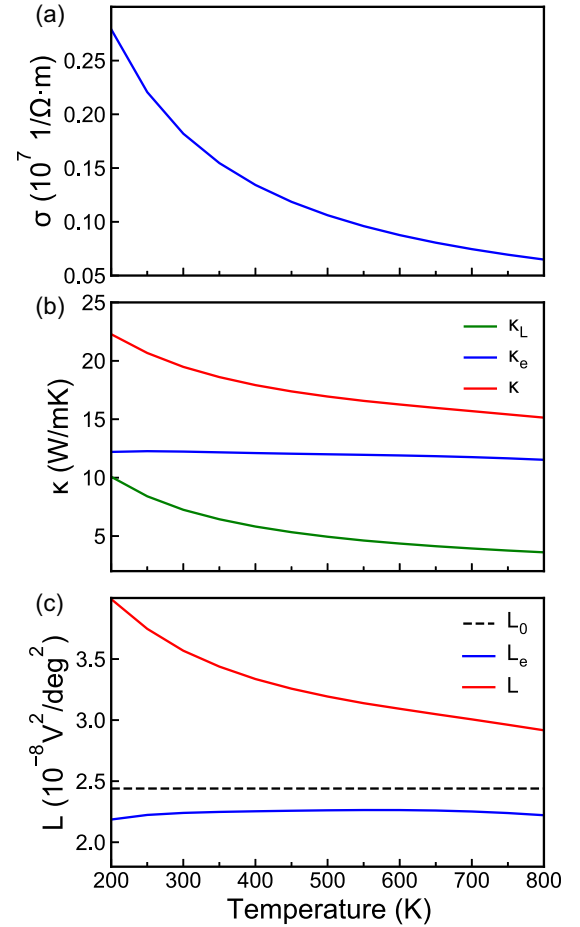


FIG. 9. (a) The electrical conductivity, (b) the κ_L , κ_e , and total thermal conductivity ($\kappa = \kappa_L + \kappa_e$), and (c) the Lorenz number as a function of temperature.

conductivity σ shows the behavior of typical metal with a decreasing trend as temperature increases. At room temperature, the calculated σ is close to $0.2 \times 10^7 \text{ S/m}$, which is expected to be verified by experiments. Note that only the el-ph scattering mechanism is considered in the σ calculation here. In fact, any defects in the experiment sample, such as impurities, could further reduce σ below the theoretical value corresponding to the intrinsic upper limit, especially at low temperatures. The electronic thermal conductivity is directly related to electrical conductivity via the WFL, with the electronic Lorenz number $L_e = \kappa_e/\sigma T$. As shown in Fig. 9(c), the calculated L_e decreases slowly with increasing temperature, and is smaller than the Sommerfeld value L_0 by $\sim 10\%$ within the whole temperature range. Surprisingly, when adding the lattice contribution κ_L to κ , the resulting Lorenz number L shows a strong dependence on temperature, and is markedly larger than the Sommerfeld value L_0 , especially at lower temperatures. This abnormally large deviation of L from L_0 is entirely ascribed to the significant lattice contribution to κ in ScZn. It enlightens us that extracting thermal conductivity from the measured electrical conductivity σ by the WFL is not reliable in metals, assuming their lattice contribution to be negligible.

IV. CONCLUSIONS

In summary, we have established a fundamental understanding of the thermal transport by phonons and electrons in ScZn from first-principles calculations. Anharmonic phonon renormalization is found crucial in determining the finite-temperature phonon energies and κ_L , and results in noticeable phonon hardening in the overall phonon spectrum. This is attributable to the strong fourth-order phonon anharmonicity, which manifests in the deep-flat U-shaped PESs and the increased squared phonon frequency with temperature caused by the loop self energy. By using the state-of-the-art computational formalism, we explore the phonon thermal transport in ScZn, taking into account the phonon renormalization, 3ph, 4ph, isotope, and ph-el scatterings. Our calculation shows that temperature-induced anharmonic effects substantially increase the κ_L relative to the HA treatment, with a twofold increase of κ_L at room temperature. This is a consequence of the large reduction in phonon scattering rates, stemming from the hardening of acoustic phonons and weakening of fourth-order anharmonicity. Moreover, by comparing the electronic and lattice contributions to κ , we find that although the calculated κ_L is secondary to the electronic contribution in the

entire temperature range, it still has a large contribution, close to 60% of κ_e at 300 K. Consequently, the large κ_L results in the abnormally large Lorenz number and its strong dependence on temperature, substantially deviated from the expected Sommerfeld constant. These findings highlight the significance of treatment of full anharmonic effects in accurately predicting the thermal transport properties of metals.

ACKNOWLEDGMENTS

This work was supported by the National Natural Science Foundation of China (NSFC, Grants No. 12374038, No. 1222402, and No. 12347101) and the Chongqing Natural Science Foundation (Grant No. CSTB2023NSCQ-JQX0024). X.Y. acknowledges support from the Fundamental Research Funds for the Central Universities of China (Grant No. 2023CDJKYJH104) and the Chongqing Natural Science Foundation (Grant No. CSTB2022NSCQ-MSX0834). Z.C. acknowledges support from the Fundamental Research Fund for Zhejiang Ocean University (Grant No. JX6311181423). Simulations have been performed at the Hefei Advanced Computing Center.

-
- [1] L. E. Bell, Cooling, heating, generating power, and recovering waste heat with thermoelectric systems, *Science* **321**, 1457 (2008).
 - [2] N. P. Padture, M. Gell, and E. H. Jordan, Thermal barrier coatings for gas-turbine engine applications, *Science* **296**, 280 (2002).
 - [3] L. Lindsay, C. Hua, X. Ruan, and S. Lee, Survey of ab initio phonon thermal transport, *Mater. Today Phys.* **7**, 106 (2018).
 - [4] X. Qian, J. Zhou, and G. Chen, Phonon-engineered extreme thermal conductivity materials, *Nat. Mater.* **20**, 1188 (2021).
 - [5] Z. Tong, S. Li, X. Ruan, and H. Bao, Comprehensive first-principles analysis of phonon thermal conductivity and electron-phonon coupling in different metals, *Phys. Rev. B* **100**, 144306 (2019).
 - [6] C. Li, N. K. Ravichandran, L. Lindsay, and D. Broido, Fermi surface nesting and phonon frequency gap drive anomalous thermal transport, *Phys. Rev. Lett.* **121**, 175901 (2018).
 - [7] Y. Chen, J. Ma, and W. Li, Understanding the thermal conductivity and Lorenz number in tungsten from first principles, *Phys. Rev. B* **99**, 020305(R) (2019).
 - [8] A. Kundu, J. Ma, J. Carrete, G. Madsen, and W. Li, Anomalous large lattice thermal conductivity in metallic tungsten carbide and its origin in the electronic structure, *Mater. Today Phys.* **13**, 100214 (2020).
 - [9] A. Kundu, X. Yang, J. Ma, T. Feng, J. Carrete, X. Ruan, G. K. H. Madsen, and W. Li, Ultrahigh thermal conductivity of θ -phase Tantalum Nitride, *Phys. Rev. Lett.* **126**, 115901 (2021).
 - [10] A. Kundu, Y. Chen, X. Yang, F. Meng, J. Carrete, M. Kabir, G. K. H. Madsen, and W. Li, Electron-induced nonmonotonic pressure dependence of the lattice thermal conductivity of θ -TaN, *Phys. Rev. Lett.* **132**, 116301 (2024).
 - [11] W. Li, Electrical transport limited by electron-phonon coupling from Boltzmann transport equation: An *ab initio* study of Si, Al, and MoS₂, *Phys. Rev. B* **92**, 075405 (2015).
 - [12] X. Yang, A. Jena, F. Meng, S. Wen, J. Ma, X. Li, and W. Li, Indirect electron-phonon interaction leading to significant reduction of thermal conductivity in graphene, *Mater. Today Phys.* **18**, 100315 (2021).
 - [13] X. Yang, Z. Liu, F. Meng, and W. Li, Tuning the phonon transport in bilayer graphene to an anomalous regime dominated by electron-phonon scattering, *Phys. Rev. B* **104**, L100306 (2021).
 - [14] T. Feng, L. Lindsay, and X. Ruan, Four-phonon scattering significantly reduces intrinsic thermal conductivity of solids, *Phys. Rev. B* **96**, 161201(R) (2017).
 - [15] X. Yang, T. Feng, J. Li, and X. Ruan, Stronger role of four-phonon scattering than three-phonon scattering in thermal conductivity of III-V semiconductors at room temperature, *Phys. Rev. B* **100**, 245203 (2019).
 - [16] Y. Xia, V. I. Hegde, K. Pal, X. Hua, D. Gaines, S. Patel, J. He, M. Aykol, and C. Wolverton, High-throughput study of lattice thermal conductivity in binary rocksalt and zinc blende compounds including higher-order anharmonicity, *Phys. Rev. X* **10**, 041029 (2020).
 - [17] X. Yang, T. Feng, J. Li, and X. Ruan, Evidence of fifth- and higher-order phonon scattering entropy of zone-center optical phonons, *Phys. Rev. B* **105**, 115205 (2022).
 - [18] B. Wei, Y. Li, W. Li, K. Wang, Q. Sun, X. Yang, D. L. Abernathy, Q. Gao, C. Li, J. Hong *et al.*, High-order phonon anharmonicity and thermal conductivity in GaN, *Phys. Rev. B* **109**, 155204 (2024).
 - [19] Y. Xia, Revisiting lattice thermal transport in PbTe: The crucial role of quartic anharmonicity, *Appl. Phys. Lett.* **113**, 073901 (2018).

- [20] T. Feng, X. Yang, and X. Ruan, Phonon anharmonic frequency shift induced by four-phonon scattering calculated from first principles, *J. Appl. Phys.* **124**, 145101 (2018).
- [21] Q. Wang, Z. Zeng, and Y. Chen, Revisiting phonon transport in perovskite SrTiO₃: Anharmonic phonon renormalization and four-phonon scattering, *Phys. Rev. B* **104**, 235205 (2021).
- [22] X. Yang, J. Tiwari, and T. Feng, Reduced anharmonic phonon scattering cross-section slows the decrease of thermal conductivity with temperature, *Mater. Today Phys.* **24**, 100689 (2022).
- [23] Y. Xia, K. Pal, J. He, V. Ozoliņš, and C. Wolverton, Particlelike phonon propagation dominates ultralow lattice thermal conductivity in crystalline Ti₃VSe₄, *Phys. Rev. Lett.* **124**, 065901 (2020).
- [24] Z. Han, X. Yang, S. E. Sullivan, T. Feng, L. Shi, W. Li, and X. Ruan, Raman linewidth contributions from four-phonon and electron-phonon interactions in graphene, *Phys. Rev. Lett.* **128**, 045901 (2022).
- [25] J. Zheng, D. Shi, Y. Yang, C. Lin, H. Huang, R. Guo, and B. Huang, Anharmonicity-induced phonon hardening and phonon transport enhancement in crystalline perovskite BaZrO₃, *Phys. Rev. B* **105**, 224303 (2022).
- [26] J. Zheng, C. Lin, C. Lin, G. Hautier, R. Guo, and B. Huang, Unravelling ultralow thermal conductivity in perovskite Cs₂AgBiBr₆: dominant wave-like phonon tunnelling and strong anharmonicity, *npj Comput. Mater.* **10**, 30 (2024).
- [27] J. Li, J. Liu, S. A. Baronett, M. Liu, L. Wang, R. Li, Y. Chen, D. Li, Q. Zhu, and X.-Q. Chen, Computation and data driven discovery of topological phononic materials, *Nat. Commun.* **12**, 1204 (2021).
- [28] G. Kresse and J. Hafner, Ab initio molecular dynamics for open-shell transition metals, *Phys. Rev. B* **48**, 13115 (1993).
- [29] G. Kresse and J. Furthmüller, Efficient iterative schemes for ab initio total-energy calculations using a plane-wave basis set, *Phys. Rev. B* **54**, 11169 (1996).
- [30] J. P. Perdew, K. Burke, and M. Ernzerhof, Generalized gradient approximation made simple, *Phys. Rev. Lett.* **77**, 3865 (1996).
- [31] P. E. Blöchl, Projector augmented-wave method, *Phys. Rev. B* **50**, 17953 (1994).
- [32] A. Togo, First-principles phonon calculations with Phonopy and Phono3py, *J. Phys. Soc. Jpn.* **92**, 012001 (2023).
- [33] W. Li, J. Carrete, N. A. Katcho, and N. Mingo, ShengBTE: A solver of the boltzmann transport equation for phonons, *Comput. Phys. Commun.* **185**, 1747 (2014).
- [34] Z. Han, X. Yang, W. Li, T. Feng, and X. Ruan, Four-Phonon: An extension module to ShengBTE for computing four-phonon scattering rates and thermal conductivity, *Comput. Phys. Commun.* **270**, 108179 (2022).
- [35] P. Giannozzi, S. Baroni, N. Bonini, M. Calandra, R. Car, C. Cavazzoni, D. Ceresoli, G. L. Chiarotti, M. Cococcioni, I. Dabo *et al.*, QUANTUM ESPRESSO: a modular and open-source software project for quantum simulations of materials, *J. Phys.: Condens. Matter* **21**, 395502 (2009).
- [36] D. Vanderbilt, Soft self-consistent pseudopotentials in a generalized eigenvalue formalism, *Phys. Rev. B* **41**, 7892 (1990).
- [37] A. Dal Corso, Pseudopotentials periodic table: From H to Pu, *Comput. Mater. Sci.* **95**, 337 (2014).
- [38] S. Poncé, E. R. Margine, C. Verdi, and F. Giustino, EPW: Electron-phonon coupling, transport and superconducting properties using maximally localized wannier functions, *Comput. Phys. Commun.* **209**, 116 (2016).
- [39] J.-J. Zhou, J. Park, I.-T. Lu, I. Maliyov, X. Tong, and M. Bernardi, Perturbo: A software package for ab initio electron-phonon interactions, charge transport and ultrafast dynamics, *Comput. Phys. Commun.* **264**, 107970 (2021).
- [40] I. Errea, B. Rousseau, and A. Bergara, Anharmonic stabilization of the high-pressure simple cubic phase of calcium, *Phys. Rev. Lett.* **106**, 165501 (2011).
- [41] T. Tadano and S. Tsuneyuki, Quartic anharmonicity of rattlers and its effect on lattice thermal conductivity of clathrates from first principles, *Phys. Rev. Lett.* **120**, 105901 (2018).
- [42] T. Tadano and S. Tsuneyuki, Self-consistent phonon calculations of lattice dynamical properties in cubic SrTiO₃ with first-principles anharmonic force constants, *Phys. Rev. B* **92**, 054301 (2015).
- [43] J. Zheng, D. Shi, S. Liu, Y. Yang, C. Lin, Z. Chang, R. Guo, and B. Huang, Effects of high-order anharmonicity on anomalous lattice dynamics and thermal transport in fully filled skutterudite YbFe₄Sb₁₂, *Phys. Rev. Mater.* **6**, 093801 (2022).
- [44] T. Tadano and W. A. Saidi, First-principles phonon quasiparticle theory applied to a strongly anharmonic halide perovskite, *Phys. Rev. Lett.* **129**, 185901 (2022).
- [45] Y. Xia, V. Ozoliņš, and C. Wolverton, Microscopic mechanisms of glasslike lattice thermal transport in cubic Cu₁₂Sb₄S₁₃ tetrahedrites, *Phys. Rev. Lett.* **125**, 085901 (2020).
- [46] O. Hellman and I. A. Abrikosov, Temperature-dependent effective third-order interatomic force constants from first principles, *Phys. Rev. B* **88**, 144301 (2013).
- [47] O. Hellman, I. A. Abrikosov, and S. I. Simak, Lattice dynamics of anharmonic solids from first principles, *Phys. Rev. B* **84**, 180301(R) (2011).
- [48] N. Shulumba, O. Hellman, and A. J. Minnich, Lattice thermal conductivity of polyethylene molecular crystals from first-principles including nuclear quantum effects, *Phys. Rev. Lett.* **119**, 185901 (2017).
- [49] W. Walukiewicz, L. Lagowski, L. Jastrzebski, M. Lichtensteiger, and H. C. Gatos, Electron mobility and free-carrier absorption in GaAs: Determination of the compensation ratio, *J. Appl. Phys.* **50**, 899 (1979).
- [50] T. Feng and X. Ruan, Quantum mechanical prediction of four-phonon scattering rates and reduced thermal conductivity of solids, *Phys. Rev. B* **93**, 045202 (2016).
- [51] S.-i. Tamura, Isotope scattering of dispersive phonons in Ge, *Phys. Rev. B* **27**, 858 (1983).
- [52] See Supplemental Material at <http://link.aps.org/supplemental/10.1103/PhysRevB.110.054304> for the phonon dispersion relation at 0 K and convergence tests with q -point meshes for lattice and electrical thermal conductivity
- [53] S. Zhou, E. Xiao, H. Ma, K. Gofryk, C. Jiang, M. E. Manley, D. H. Hurley, and C. A. Marianetti, Phonon thermal transport in UO₂ via self-consistent perturbation theory, *Phys. Rev. Lett.* **132**, 106502 (2024).
- [54] W. Zhou, Y. Dai, J. Zhang, B. Song, T.-H. Liu, and R. Yang, Effect of four-phonon interaction on phonon thermal conductivity and mean-free-path spectrum of high-temperature phase SnSe, *Appl. Phys. Lett.* **121**, 112202 (2022).
- [55] S. Wen, J. Ma, A. Kundu, and W. Li, Large lattice thermal conductivity, interplay between phonon-phonon, phonon-electron, and phonon-isotope scatterings, and electrical transport in molybdenum from first principles, *Phys. Rev. B* **102**, 064303 (2020).